The Mechanism of Excimer Formation: An Experimental and Theoretical Study on the Pyrene Dimer

Joscha Hoche[a], Hans-Christian Schmitt[a], Alexander Humeniuk, Ingo Fischer,*
Roland Mitric, and Merle I. S. Röhr*

Institut für physikalische und theoretische Chemie, Julius-Maximilians-Universität Würzburg, D-97074, Würzburg, Germany

E-mail: ingo.fischer@uni-wuerzburg.de; merle.roehr@uni-wuerzburg.de

[a] These authors contributed equally to the work.

Abstract

The understanding of excimer formation in organic materials is of fundamental importance, since it profoundly influences their functional performance in applications such as light-harvesting, photovoltaics or organic electronics. We present a joint experimental and theoretical study of the ultrafast dynamics of excimer formation in the pyrene dimer, which is the archetype of an excimer forming system. We perform simulations of the nonadiabatic photodynamics in the frame of TDDFT that reveal two distinct excimer formation pathways in the gas-phase dimer. The first pathway involves local excited state relaxation close to the initial Frank-Condon geometry that is characterized by a strong excitation of the stacking coordinate exhibiting damped oscillations with a period of 350 fs that persist for at least 5 ps. The second excimer forming pathway involves large amplitude oscillations along the parallel shift

coordinate with a period of $\approx$ 900 fs that after intramolecular vibrational energy redistribution on a 2 ps time scale leads to the formation of a perfectly stacked dimer. The electronic relaxation within the excitonic manifold is mediated by the presence of conical intersections formed between fully delocalized excitonic states. Such conical intersections may generally arise in stacked π-conjugated aggregates due to the interplay between the long-range and short-range electronic coupling. The simulations are supported by picosecond photoionization experiments in a supersonic jet that provide a time-constant for the excimer formation of around 6-8 ps, in excellent agreement with theory. Finally, in order to explore how the crystal environment influences the excimer formation dynamics we perform large scale QM/MM nonadiabatic dynamics simulations on a pyrene crystal in the framework of the tight-binding TDDFT. In contrast to the isolated dimer, the excimer formation in the crystal follows a single reaction pathway in which the initially excited parallel slip motion is strongly damped by collisions with the surrounding molecules leading to the slow excimer stabilization with a time constant of several picoseconds.

Introduction

Excimers, complexes that are only weakly associated in the electronic ground state, but interact strongly when electronically excited,[1,2] play an important role in the electronic relaxation of molecular aggregates and have also a profound influence on the functional performance of organic devices since they can act as trap sites that limit the exciton diffusion.[3–7] On the other hand it has been recently found that excimer formation can also have a positive effect on the properties of organic materials, facilitating processes such as singlet fission.[8–12] For this reason, the understanding of the excimer formation dynamics in molecular aggregates is of fundamental importance for the development of novel materials that can be employed in organic electronics or photovoltaics applications. In addition to their importance for the development of functional materials, excimers can be also employed as probes in biological molecules.[13] For example, recently long-lived excimers of nanostructures for imaging applications were reported.[14]

While the relation between the structure and spectral properties of multichromophoric assemblies is by now well established, there is a growing experimental evidence that ultrafast nonadiabatic relaxation processes play a fundamental role in determining their functionality.[15,16] In multichromophoric assemblies such as those formed by self-assembly of π-conjugated molecular dyes, even a minimal change of the structural parameters can significantly change the efficiency of nonradiative relaxation processes. The coupling between the chromophores in such superstructures can give rise to novel funnels between the delocalized exciton- or charge transfer states that enhance the nonradiative relaxation and limit their functionality, similar to the well established role which conical intersections play in molecular photochemistry. The appearance of such funnels is determined by the interplay between the long-range and short-range electronic coupling. The latter is critically dependent on the orbital overlap between the building blocks and may lead to ultrafast excimer formation which often competes with the transport and can destroy the function even in seemingly perfect structures.

In this paper, we undertake a joint theoretical and experimental effort in order to reveal the mechanism of excimer formation in pyrene dimer. This system represents a prototype of an excimer forming aggregate, and it was the first aromatic system for which excimer behavior was observed.[17] We employ large scale nonadiabatic dynamics simulations in the frame of time-dependent density functional theory (TDDFT) in order to explore the coupled electron-nuclear dynamics that sets in after the electronic excitation and to identify the relaxation channels and the time-scales of relevant processes. In addition to the study of the pyrene dynamics in the gas phase, we perform also simulations on a crystal model which allow us to address the influence of the crystal environment on the excimer formation dynamics. Experimentally, we use picosecond time-resolved photoionization spectroscopy in supersonically cooled jets to study the intrinsic properties of excimers without external perturbations.[18] Notice that previously the time constants for the excimer formation on the picosecond scale were measured in liquid benzene[19] but additional phenomena caused by the interaction with the solvent molecules were present that impeded the data interpretation.

From the experimental point of view, excimers are commonly identified by a characteristic red-shifted fluorescence with a lifetime on the order of several ns which has by now been observed for a number of aromatic molecules. For example, in an early study Saigusa and Lim observed rise times of 36 ps and 46 ps in time-resolved fluorescence studies on fluorene and dibenzofurane clusters and assigned them to excimer formation.[20] However, fluorescence studies lack mass resolution, which is essential in cluster experiments. In this context, the time-resolved photoionization represents a viable alternative. Although it cannot detect the characteristic red-shifted emission, it provides information on cluster size distribution and possibly on cluster fragmentation. It is therefore well suited for real-time studies of intracluster dynamics.[21–25] Recently the so far most detailed investigation on the excited-state dynamics and excimer formation in molecular dimers was reported by Miyazaki and Fujii for the benzene dimer.[26] These authors extracted time constants of 18 ps and 10 ps for the excimer formation from the S_1 origin and the S_1 6^1 vibrational level. A relevant

factor in experiments on benzene is the fact that the dimer has a T-shaped minimum energy geometry. The excited state dynamics thus corresponds to a rearrangement of a locally T-shaped structure to the parallel sandwich-type structure of the excimer. In contrast to benzene dimer, pyrene dimer exhibits a face-to-face orientation in the electronic ground state that is also characteristic to the arrangement of π-conjugated molecules in a wide variety of molecular crystals and supramolecular aggregates. Note that the exact mechanism of excimer formation of pyrene is still controversial. While it is generally believed that in solution an excimer is formed in a diffusion-controlled reaction of an excited singlet molecule with a ground-state molecule,[27] other work concluded that it originates from two pre-oriented pyrene molecules.[28] The aim of our experimental and theoretical study is to provide for the first time the full dynamical picture of the excimer formation mechanism.

Computational methods

Electronic structure and nonadiabatic dynamics in the gas phase. The electronic structure of the pyrene dimer has been described in the framework of the density functional theory employing the hybrid BH-LYP functional with 50 % Hartree-Fock exchange[29–31] combined with the triple-zeta valence plus polarization (TZVP) basis set.[32] In order to include the dispersion interaction the GD3 correction was used.[33] It has been shown previously[34] that this level of theory reasonably well describes ground and excited state properties of pyrene dimer. The electronically excited states and the nonadiabatic dynamics simulations of excimer formation have been performed in the frame of the time-dependent density functional theory (TDDFT). Due to the computational demand, nonadiabatic dynamics simulations have been performed using a smaller def2-SVP[35] basis set, which offers a good compromise between accuracy and computational cost. For all TDDFT calculations, the TURBOMOLE 6.3 suite of programs was used.[36] The initial conditions for the excited state nonadiabatic dynamics simulations have been sampled from a 20 ps long ground state MD simulation

at constant temperature of 50 K. The nonadiabatic dynamics has been simulated using the trajectory surface hopping method implemented in the framework of TDDFT.[37–40] In the simulation the electronic ground state and the first two singlet excited states were included. The classical Newtonian equations of motion for the nuclear dynamics were solved using the velocity Verlet algorithm with a time step of 0.2 fs. The electronic Schrödinger equation along the classical trajectories has been solved using the Runge-Kutta method with energies, gradients and nonadiabatic couplings calculated from TDDFT.[37–40] Since only scalar nonadiabatic couplings are available in the frame of TDDFT, the energy conservation has been imposed by uniformly rescaling velocities after a successful hop.

QM/MM nonadiabatic dynamics in crystal environment. In order to simulate the excited state nonadiabatic dynamics of a pyrene dimer in a crystal the following setup is used: The pyrene crystal unit cell is enlarged by duplicating the minimal unit cell along all three axes until an entire pyrene dimer is contained in the supercell. The total system is partitioned into an inner region containing the central dimer I, which is treated quantum mechanically within tight-binding DFT (QM part) and an outer region O, which is described using the DREIDING force field[41] with periodic boundary conditions (MM part). The total energy is computed using a subtractive scheme:

$$E = E_{MM}(I + O) + E_{QM}(I) - E_{MM}(I) \tag{1}$$

where E_{MM} includes all energy terms of the force field except for the non-bonded electrostatic term. Since hydrogen and carbon have similar electronegativities the partial charges in pyrene are small, so that the electrostatic interactions in the MM calculations can be neglected. The small polarization of the QM part by the partial charges in the MM part is also ignored. In the MM calculation periodic boundary conditions are applied so that atoms on one end of the supercell are in contact with atoms on the opposite side through bonding or non-bonding interactions. This ensures that the shape of the periodic supercell is

not distorted during the dynamics. The electronic structure of the inner region is described using non-periodic tight-binding DFT, so discrete electronic energy levels result rather than continuous bands, which are present in a crystal. The initial conditions for 50 trajectories were generated by assigning random velocities to the nuclei. The resulting trajectories were propagated for 1 ps on the ground state at a constant temperature of 50 K to obtain an equilibrated ensemble. Then all trajectories were lifted adiabatically to the S_1 state and allowed to evolve for another 5 ps. This simulates the situation where the central pyrene dimer is excited and all other dimers are in the ground state. No electronic coupling exists between the different dimers but vibrational energy can flow from the central dimer to the crystal.

Experimental methods

Pyrene was obtained commercially from Sigma-Aldrich and used without further purification. The samples were placed in an oven attached to a pulsed solenoid valve and heated to around 160 °C. The evaporated pyrene molecules were seeded in Argon and expanded into a differentially pumped vacuum chamber through a 1.0 mm diameter nozzle to obtain a cooled molecular beam. The skimmed jet entered the experimental chamber with a pressure of 5.0 - 8.5 $\times 10^{-7}$ mbar. The detailed setup of the apparatus has been described in a previous publication.[42] In the experimental chamber the molecules were ionized by a picosecond laser with a repetition rate of 10 Hz. The details of the laser system, consisting of a solid state Nd:YLF (neodymium-doped yttrium lithium fluoride) laser and an optical parametric generator (OPG), are also given elsewhere.[43] In most experiments described below the tunable OPG output was used as the pump beam, while a small part of either the 2^{nd} (527 nm) or 3^{rd} (351 nm) harmonic of the Nd:YLF laser (200 - 300 J) was sent over a motorized linear translation stage and used as the probe pulse. The OPG output between 330 and 370 nm yielded pulses with a bandwidth of approx. 20-25 cm^{-1} and a pulse energy of 30 to 150 μJ.

The instrument response function (IRF) was determined to be around 4 ps. Measurements at an excitation wavelengths of 351 nm, which is the point of degeneracy of the OPG, were conducted using the Nd:YLF laser 3^{rd} harmonic as the pump and the 2^{nd} harmonic as the probe. Pump and probe pulses were overlapped in front of the experimental chamber using a dichroic mirror. Unfocused pulses yielded the best signal-to-noise ratio (SNR). Ions were accelerated in a TOF mass spectrometer onto a multichannel plate (MCP) detector. The data were averaged for at least 50 shots per point for every scan, 5 to 15 scans were averaged to receive a good signal-to-noise ratio.

Results and discussion

REMPI-spectra. Fluorescence excitation spectra of pyrene and its dimer have been recorded before in free jets.[44,45] The origin of the $S_1(^1B_{2u}) \leftarrow S_0(^1A_{1g})$ transition of the monomer was observed at 367.4 nm,[44,46] while the origin of the strongly vibronically coupled S_2 state, is observed at 321.5 nm.[44] The dimer $(Py)_2$ exhibits a broad and unstructured electronic spectrum that sets in around 370 nm.[45] These earlier frequency-domain studies guided the present time-domain experiments.

Resonance-enhanced multiphoton ionization spectra (MPI) of pyrene monomer were recorded by tuning the ps OPG. The adiabatic ionization energy (IE) of neutral pyrene was determined to be 59888 cm^{-1} (7.425 eV),[47] so the molecule can be ionized in a [1+1] process. Two selected spectra, corresponding to the origin regions of the S_1 $(^1B_{2u}) \leftarrow S_0$ $(^1A_{1g})$ and the $S_2 \leftarrow S_0$ transition are given as Fig. S1 and S2 in the electronic supplementary information (ESI). As can be seen, individual transitions into low-lying vibrational bands of the S_1 state can be resolved. They have been assigned before to a_g and vibronically induced b_{3g} vibrations.[44] The close-lying bands at the S_2 origin around 320 nm-322 nm, however cannot be separated due to the 20-25 cm^{-1} bandwidth of our ps-laser system. In the dimer mass channel only a broad band, starting around 370 nm was observed (see Fig. 1),

again in agreement with earlier work. In Fig. 1 we also compare the experimental spectrum with theoretical simulations for a thermal ensemble that has been used to run nonadiabatic dynamics simulations (see below). As can be seen, the onset of the absorption as well as the shape of the first peak are almost perfectly reproduced by theoretical simulations.[45]

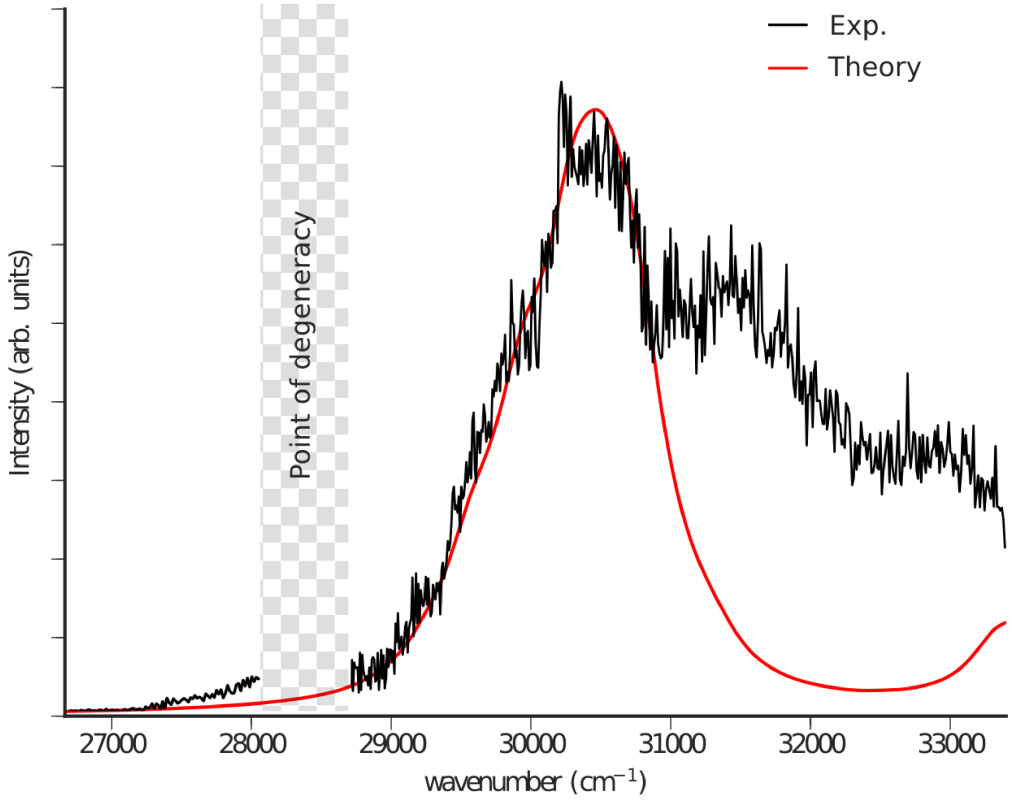

Figure 1: [1 + 2] -REMPI of the pyrene dimer and simulated absorption spectra (red), shifted by 1290 cm^{-1} (0.16 eV) to lower energies to match the experimental maximum absorption peak. A broad band starting around 27000 cm^{-1} is visible. Note that the point of degeneracy of the ps laser-system used in this study is located at 351 nm(28490 cm^{-1}). Due to the low laser power no signals could be recorded around this point.

Mass spectra. A challenge in all cluster experiments is the finite size distribution one generally has to deal with. When the electronic spectrum is sufficiently resolved, one can often ionize a particular cluster size selectively. For clusters with broad and unstructured bands this is not possible. As fragmentation of larger clusters can obscure signals in the lower mass channels, it is necessary to select a narrow size distribution by choosing suitable expansion conditions, i.e. by varying the sample temperature and the seed gas pressure. Fig.

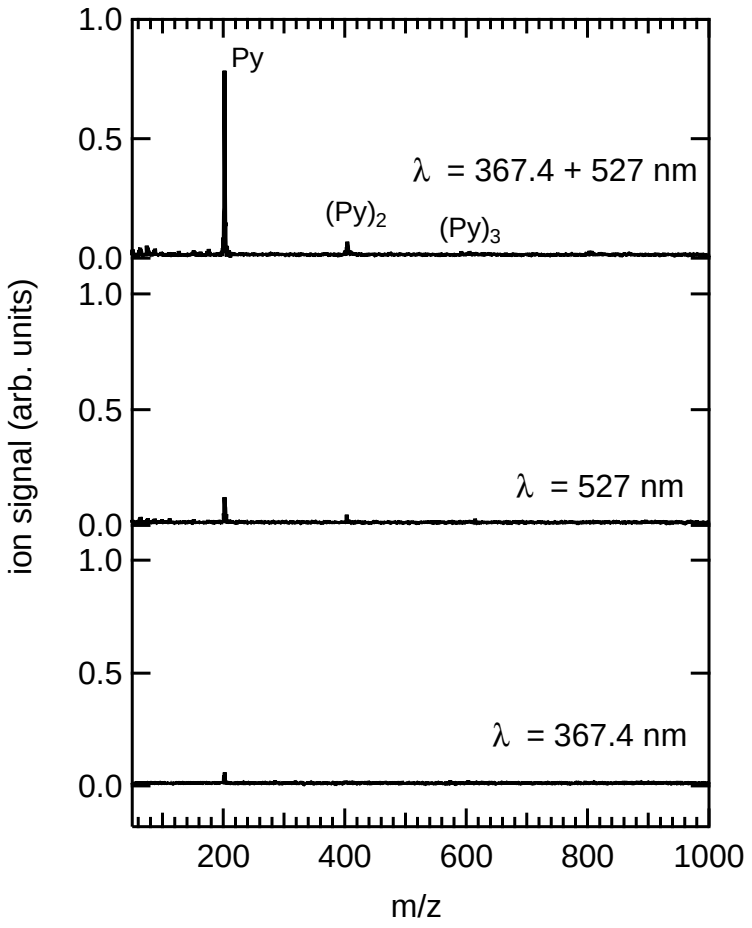

Figure 2: Mass Spectra of pyrene, recorded at zero time delay between pump and probe laser (top trace). All spectra are dominated by the monomer. At 527 nm (probe only) there is a small one-color background signal in the dimer mass channel (center trace). At 367.4 nm (pump only) the dimer background signal is negligible (bottom trace).

2 shows mass spectra that were recorded at 367.4 nm, close to the S_1 origin of the pyrene monomer. The second harmonic of the Nd:YLF laser at 527 nm was chosen as the ionization wavelength. As can be seen, the monomer signal dominates the mass spectrum under all conditions. A dimer signal is clearly visible, while higher clusters appear with only small intensity. The probe only (527 nm) spectrum yields a background signal due to multiphoton ionization. Small signals at low masses indicate that some dissociative photoionization is present. The pump only (367.4 nm) spectrum on the other hand shows no background from clusters.

Experiments at the S_2 Origin of the Pyrene Monomer. The spectrum around the S_2 origin (see Fig. S2 for a wavelengths scan) is considered to be an example for intermediate level structure, i.e. an individual bright zero order state of S_2 is coupled to a limited number of vibrational levels in S_1. An extensive simulation of the fluorescence excitation spectrum, taking vibronic coupling into account has already been presented.[46] Due to the bandwidth of our ps-laser several eigenstates (probably five to ten) are excited around 320.6 nm. The pump-probe signal (see Fig. S4) decays rapidly to a constant level. A fit to the data yields 3.1 ps. Given the 5 ps IRF of our setup, this is the ultimate limit for a time constant that can be extracted from our experiments. The signal decay is due to the redistribution of vibrational energy (IVR) from the S_2 zero order state to the first tier of S_1 levels as has been described in.[44]

Time-Delay Scans of the Pyrene Dimer. After characterizing the spectrum by MPI, we recorded time-delay scans at various wavelengths to gain insight into the dynamics of the pyrene dimer, $(Py)_2$. As the clusters show broad and unstructured absorption bands, selective excitation of one mass is not possible. Under these circumstances dissociative photoionization is a major obstacle in cluster experiments, because dynamics in a larger cluster can erroneously appear in a lower mass channel as discussed previously.[24] It is therefore necessary to discuss the relevant ionization and fragmentation thresholds. In a recent synchrotron radiation photoionization experiment ([48]) IEs of 6.95 eV and 6.76 eV were

determined for the pyrene dimer and trimer. For the appearance energies of the clusters, values of AE(Py_2, Py^+) = 8.7 eV and AE(Py_3, Py_2^+) = 7.9 eV were found. We therefore started our investigation with a pump wavelength of 367.4 nm and a probe wavelength of 527 nm. Assuming a [1+2′] MPI scheme the total energy amounts to 8.08 eV and lies between IE(Py_2) and AE(Py_2, Py^+), thus the dimer is ionized, but dissociative ionization leading to a charged monomer is suppressed. Note that the pump wavelength is very close to the band onset and the absorption cross section is small. Fig. 3 shows selected time delay

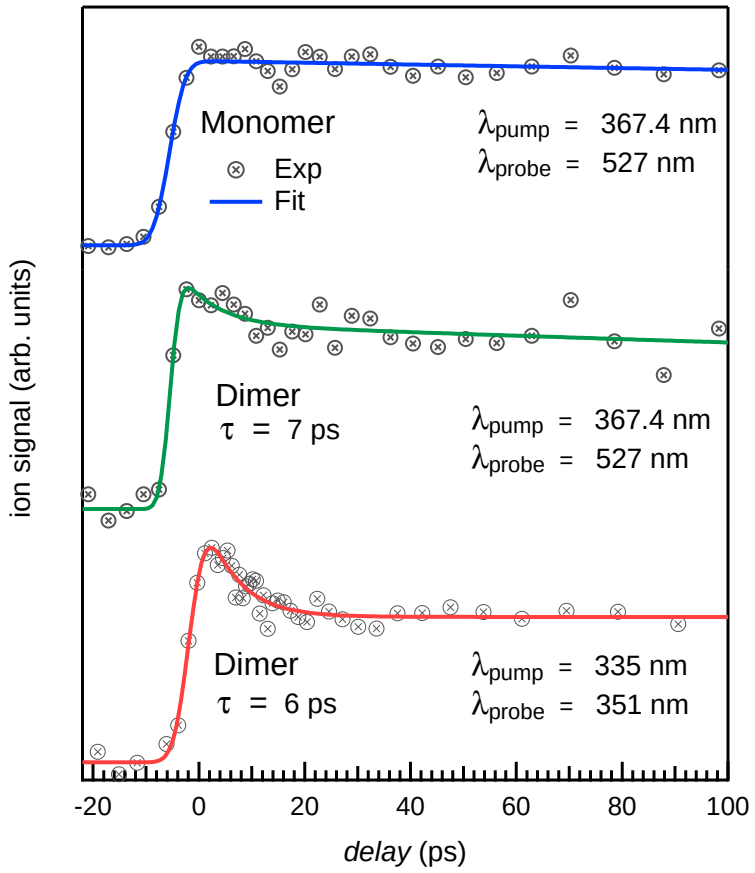

Figure 3: Selected time delay scan. Close to the S_1 band origin, the pyrene monomer shows a long lifetime (blue line), while the dimer (green line) exhibits a picosecond transient. This transient, which decays to a constant offset, becomes more pronounced at 335 nm excitation (red line), close to the absorption maximum of the dimer.

scans. The monomer signal (top trace, blue line) shows a step function, in agreement with

the nanosecond lifetime reported previously, thus fragmentation of the dimer is successfully suppressed. The dimer signal in the center trace (green line) exhibits an initial decay with a time constant ≈7 ps to a relatively large offset. When the probe beam was slightly focused, signal levels increased significantly, but considerable fragmentation became visible. Note that the total energy in a [1+2′] scheme is slightly above AE(Py_3, Py_2^+) = 7.9 eV, so dissociative ionization of the trimer is in principle possible. It would however lead to a signal increase in the dimer channel with time. Nevertheless it is therefore important to reduce the concentration of larger clusters in the beam considerably. As visible in Fig. 1, the trimer signal is negligible under our experimental conditions. At larger pump wavelengths (λ>367.4 nm) signals were too small to record pump-probe spectra with sufficient signal to noise (S/N) ratio. The maximum of the dimer absorption band is measured around 335 nm. We therefore conducted further time-resolved experiments at this pump wavelength, using a 351 nm probe. As the dimer itself absorbs substantially at 351 nm, the probe beam had to be attenuated until the background signal was negligible. This [1+1] process deposits a total energy of 7.23 eV in the cluster, so a dissociative ionization of the trimer is not possible, in agreement with the energetics discussed above. The resulting time-delay scan is depicted in the bottom trace of Fig. 3 The initial transient is more pronounced than at 367.4 nm, but the time constant of the fit (red line) is only slightly shorter, around 6 ps. Again the signal decays to a large offset level. Further experiments were carried out at 351 nm pump, employing probe wavelengths of 400 nm and 527 nm. The two spectra recorded with perpendicular and parallel polarization of pump- and probe-laser are given in Fig. S5 and show very similar lifetimes of 6-7 ps, which indicates that the observed transient is not related to molecular rotation.

Since dissociative photoionization of the dimer can also be neglected as the source of the transient in the dimer channel as discussed above, the observed dynamics with a time constant of 6-8 ps has to be linked with dynamics in the electronically excited state of the neutral dimer. Furthermore, the large signal offset at long delay times rules out ionization

from the electronic ground state, which would be associated with a small ionization probability. Thus internal conversion to the ground state can also be disregarded as a deactivation pathway. This leaves a process within the electronically excited states as the source of the transient that leads to a small change in the absorption probability. Formation of an excimer, connected with a reorientation of the two pyrene units would be such a process. As the excimer is a lower energy isomer, there is excess energy available which is redistributed as vibrational energy in the cluster. At the low probe energies chosen to suppress dissociative photoionization, the ionization probability of vibrationally excited dimers is reduced, leading to a decreasing dimer ion signal. Interestingly similar time constants as in the present work were observed for emission changes from zeolite-incorporated pyrene (7-13 ps),[49] and in pyrene-doped polymers (4-10 ps).[50] In both cases these contributions were assigned to excimer formation in the respective systems. The present work on the isolated pyrene dimer seems to confirm this interpretation. We therefore carried out theoretical work to investigate the intrinsic dynamics of the pyrene dimer in more detail and validate the qualitative interpretation given above.

Table 1: Comparison between the calculated and experimental vertical transition energies and interplane separation in pyrene dimer.

	TDDFT/BH-LYP [a]			exp.[a]
	def2-SVP	6-31G*	TZVP	
interplane distance (Å)	3.38	3.42	3.46	3.75
S_1 (eV)	3.95 (bright)	4.01 (bright)	3.99 (dark)	
S_2 (eV)	3.98 (dark)	4.04 (dark)	3.99 (bright)	

[a] present work

Structural properties and excited states in pyrene-dimer. The lowest energy isomer of the pyrene dimer in the ground electronic state (S_0) exhibits a stacked structure with the distance between the molecular planes in the range between 3.38-3.46 Å(cf. Fig. 4a) calculated at the BHLYP+GD3 level of theory (cf. Table 1). In the lowest energy

structure the monomers are displaced along the long molecular axis leading to the structure with C_{2h} symmetry shown in Fig. 4a. In the following, this structure will be referred to as the parallel-displaced (PD) structure. The perfectly stacked D_{2h} isomer is in the ground state higher in energy by 0.16 eV. Upon stacking, the electronic interaction between the individual monomers leads to the formation of molecular orbitals that are delocalized over both subunits. The frontier molecular orbitals for both isomers can be derived from the frontier orbitals of the monomers and are shown in Fig. 4c and d together with their decomposition in terms of the monomer orbitals. Since the distance between the monomers is relatively small, the interaction between the monomer MOs leads to the relatively large energy splitting of the dimer orbitals. Overall, from the HOMO and LUMO orbitals of both monomers four frontier orbitals arise. The HOMO-1 and HOMO orbitals are represented by a negative and positive linear combination of the HOMO orbitals of both monomers. Notice that the HOMO-1 is destabilized with respect to the monomer due to the largely antibonding interaction in the PD structure while the HOMO orbital is stabilized. This situation reverses in the stacked structure, where the dimer HOMO is strongly destabilized and the HOMO-1 is stabilized. As can be seen, the same trend applies also to the unoccupied molecular orbitals. Thus, the parallel shift along the long molecular axis from the PD structure to the fully stacked structure leads to the overall lowering of the HOMO-LUMO gap. The excitation energies presented in Table 1 are in satisfactory agreement with the experimentally observed ones. In order to explore the change in the energies and intensities of the lowest excited states we have calculated a section from the potential energy surfaces along the parallel shift coordinate which are presented in Fig. 5. The two lowest excited states (S_1 and S_2) have dominantly Frenkel-exciton character and are almost degenerate at the Franck-Condon geometry (denoted B in Fig. 5). The character of the two lowest excited states can be seen in the $S_0 \rightarrow S_1$ transition densities calculated for three characteristic geometries along the parallel shift coordinate denoted A, B and C, in Fig. 5b. The local transition dipole moments of the individual monomers are parallel at the FC geometry (point B) corresponding to a

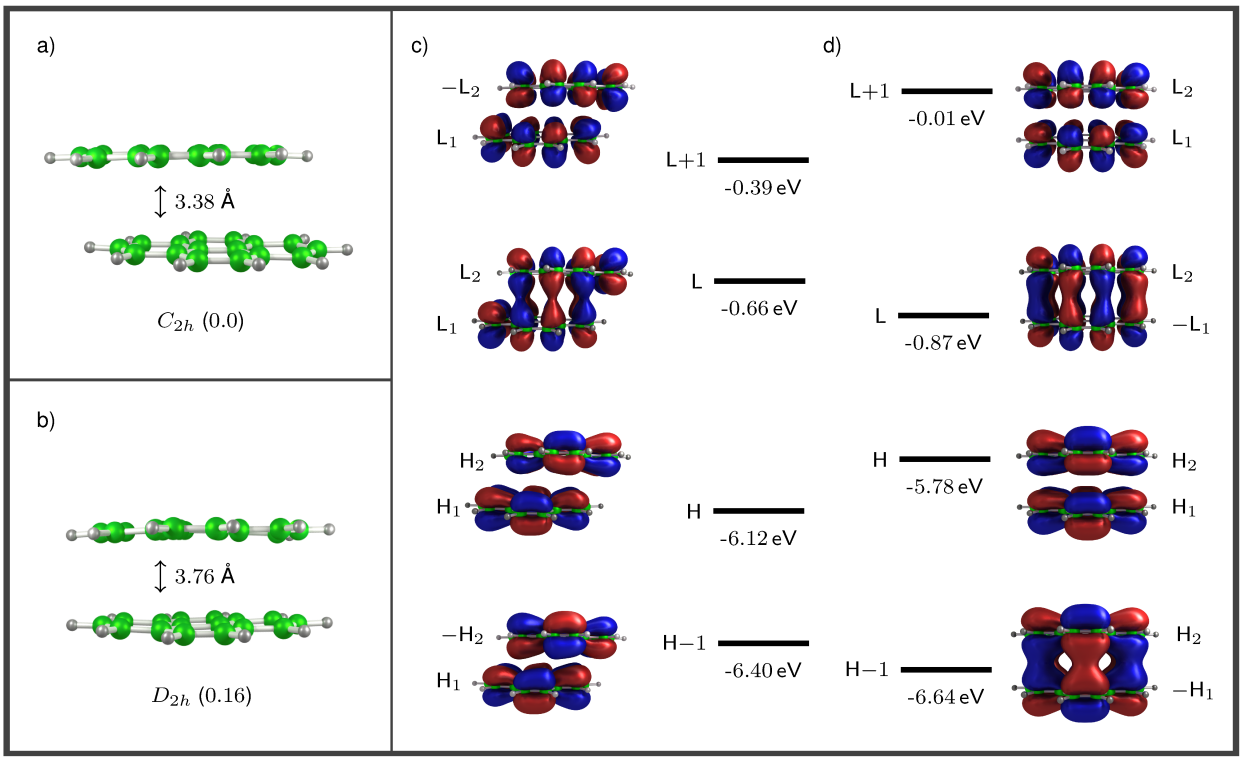

Figure 4: (a and b) Ground state geometries and energies (in eV) of the C_{2h} and D_{2h} isomers of pyrene dimer optimized at the BHLYP/def2-SVP level of theory. (c and d) Frontier orbitals of the C_{2h} and D_{2h} isomers. $\mathsf{H}_{1,2}$ and $\mathsf{L}_{1,2}$ denote the monomeric orbitals and their contribution in the dimer.

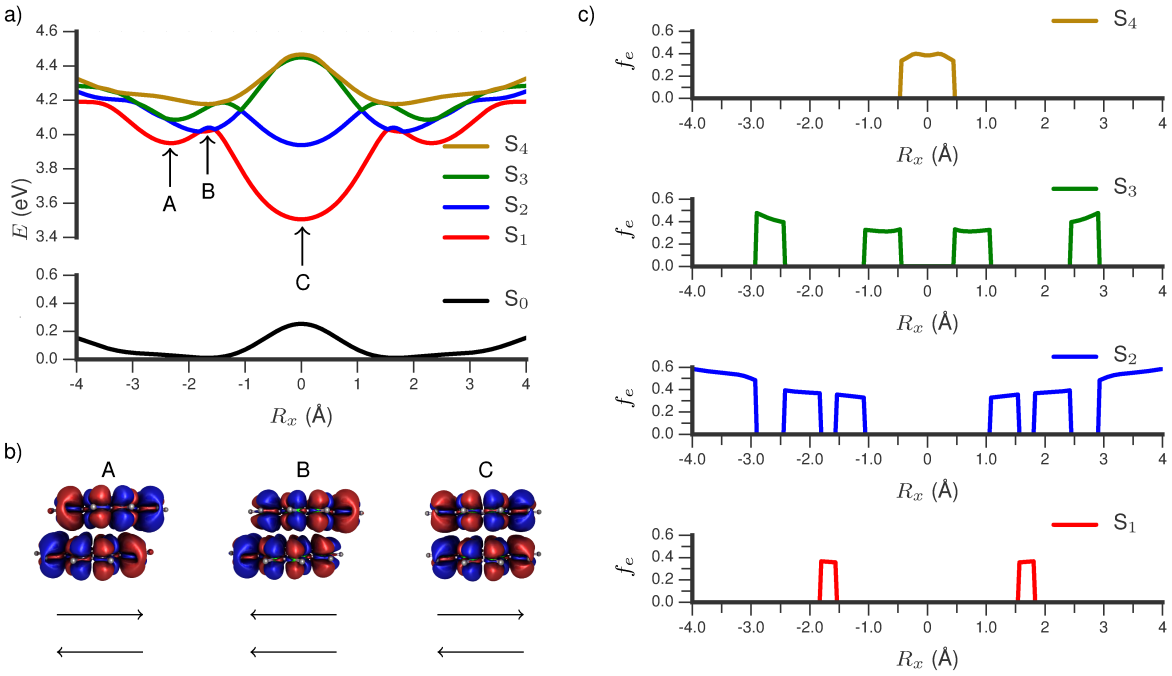

Figure 5: (a) Energies of the ground (S_0) and the four lowest ($S_1 - S_4$) excited states of the pyrene dimer along the parallel shift coordinate (R_x). The coordinate system is shown in the inset.(b) The transition densities between the ground state and the first excited states for three selected geometries denoted with A, B, C are shown in the lower part of the figure illustrating the change between the parallel and antiparallel arrangement of the monomer transition dipoles along the R_x coordinate. (c) Oscillator strength for the $S_0 \rightarrow S_i$ $i = 1 - 4$ transition along the R_x coordinate illustrating the change of the diabatic character of the excited states.

bright S_1 state. As the two monomers slide along the parallel direction the diabatic character of the S_1 and S_2 states interchange at two geometries close to the FC point which indicates the presence of a conical intersection. The lowest excited state changes from the parallel to the anti-parallel orientation of the transition dipole moments as can be seen from the transition densities at points A and C. At the perfectly stacked geometry (point C) the splitting of the excitonic state manifold is much larger than at the FC geometry and has a value of almost 0.5 eV. In order to illustrate the change of the electronic character of the lowest states the oscillator strengths of the four lowest excited states as a function of the parallel displacement are shown in the right hand side of Fig. 5. While either the S_1 and S_2 states are intense close to the FC geometry, the parallel displacement towards the stacked structure leads to the exchange of the intensities such that close to the perfectly stacked structures the higher lying states S_3 and S_4 become bright. In fact, the perfectly stacked structure is an example of the H-aggregate in which the highest lying exciton state has the whole intensity while the initial PD structure is an intermediate case between the J- and H-aggregate. The crossings between the electronic states that arise along the parallel shift coordinate may act as funnels that mediate the electronic relaxation since a strong nonadiabatic couplings will occur close to the crossing geometries mediating efficient nonradiative transitions. In the following, we will address the question how the conical intersections between excitonic states may arise as a combining effect of the long-range and short-range electronic couplings.

Conical intersections within the exciton model for the excited states of pyrene dimer. The shape of the potential energy surfaces shown in Fig. 5, the energetic splitting and the electronic character of the excited states can be understood in terms of a minimal model in which the excited states of the dimer are formed by coupling between the local excited states of the monomers and the intermolecular charge transfer states. Since the two monomers are very close together, the overlap between the electronic densities cannot be neglected so that in addition to the long-range Förster type of electronic coupling also the short-range coupling which is strongly dependent on the orbital overlap needs to be taken

into account. It has been previously shown that the short-range couplings are particularly important in flat molecules such as polycyclic aromatic hydrocarbons[51,52] that can be tightly packed.

The short-range coupling contains the contribution of the Dexter-type exchange interaction as well as the coupling to the intermolecular charge transfer states. A detailed analysis of the electronic couplings in stacked π-systems has been provided already long time ago.[53] The coupling between the lowest two states can thus be decomposed in a short- and long-range contribution according to,

$$V = V_{LR} + V_{SR}. \tag{2}$$

In order to extract the values of the long- and short-range couplings we use our ab initio calculated potential energy surfaces and calculate the long-range coupling independently by using the TrEsp procedure introduced by Madjet et al.[54] Here, atom centered transition charges are fitted in order to reproduce the electrostatic potential of the electronic transition density and the coupling is calculated as:

$$V_{LR} = \sum_{i,j} \frac{q^A_{eg,i} q^B_{eg,j}}{|\mathbf{R}^A_i - \mathbf{R}^B_j|} \tag{3}$$

where the $q^A_{eg,i}$ and $q^B_{eg,j}$ denote partial transition charges at the monomer subunits A and B and $\mathbf{R}^A_i$ and $\mathbf{R}^B_j$ are atomic position vectors for the atoms i and j belonging to different monomers. For two identical monomers the total coupling can be obtained from the adiabatic energies of the lowest two excited states that are available from the quantum chemical calculations

$$V = \frac{E_{S_2} - E_{S_1}}{2}. \tag{4}$$

Therefore, since the long-range part of the coupling can be independently calculated, the short-range part of the coupling can be extracted from Eq. 2. Notice, that this approach can be generalized to hetero-dimers as shown by Scholes et al.[55] and Madjet et al.[56]

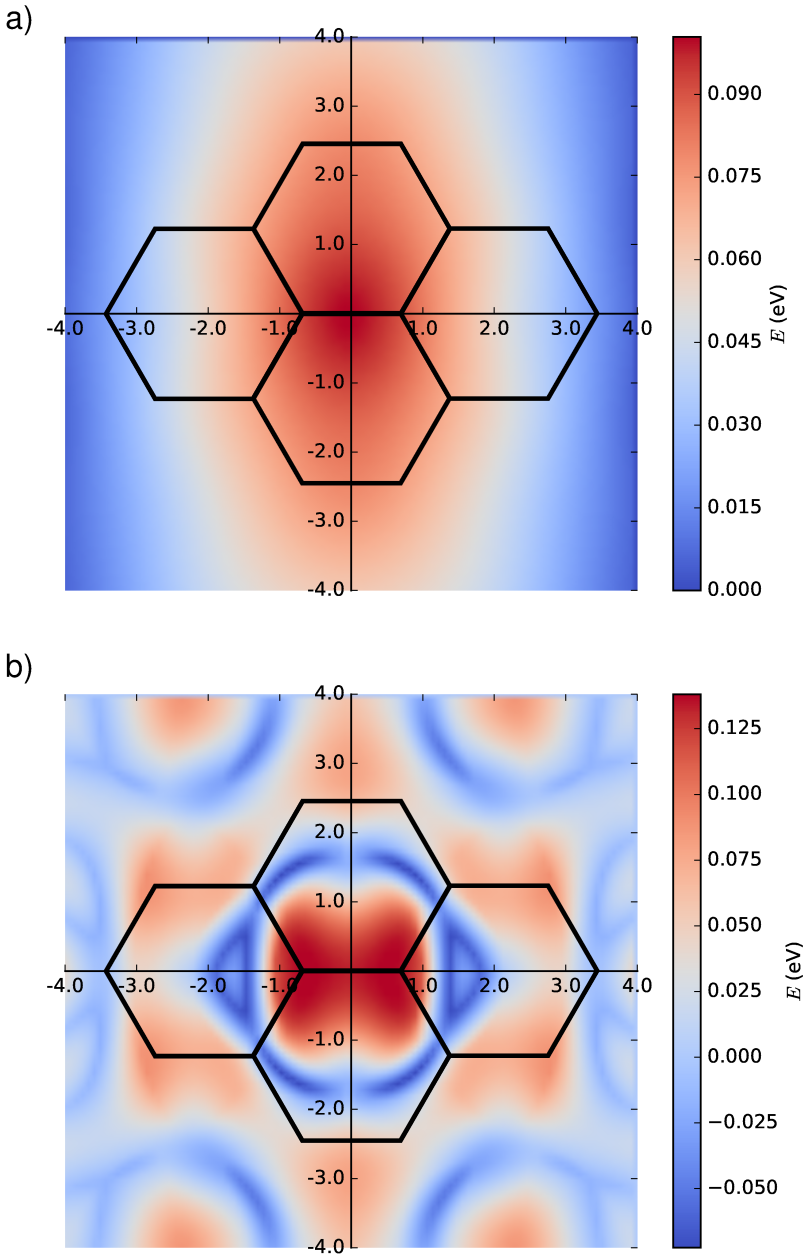

Figure 6: (a and b) Long- and short-range coupling for the parallel displacement of the pyrene monomers with fixed stacking distance of 3.3 Å.

In Fig. 6 we present calculated couplings for different relative positions of the pyrene monomers within the dimer. As can be seen from Fig. 6a the parallel displacement along the R_x and R_y coordinates leads to a smooth variation of the long-range coupling which exhibits largest value close for the perfectly stacked structure. In contrast, the short range coupling shows more complicated behavior since it changes with the orbital overlap between the two monomers which is strongly dependent on the relative position of the monomers and exhibits also sign variations (cf. Fig. 6b). The change of the sign in the short-range coupling is responsible for the change of the diabatic character of the S_1 and S_2 state at the intersection of the S_1 and S_2 states (cf. Fig. 5). In general, in dimers consisting of two identical chromophores conical intersections between the excitonic states may arise at geometries where the total coupling changes its sign and the diagonal diabatic energies become equal. Such conical intersection can lead to ultrafast electronic relaxation and their presence might have a direct influence on the functional properties of stacked molecular assemblies.

Nonadiabatic dynamics of excimer formation: Gas phase vs. crystal. In order to determine the mechanism that governs the excited state relaxation and leads to the excimer formation, we have performed trajectory surface hopping dynamics simulations in the frame of TDDFT at the BH-LYP/def2-SVP level. The two lowest excited states (S_1 and S_2) and the ground state have been included and the nonadiabatic couplings between all states has been calculated. Due to the high computational demand and relatively long simulation time of 2 ps we were only able to propagate a limited number of 20 trajectories at the highest BH-LYP level of theory. The results have been further confirmed by running more approximate long-range corrected tight-binding TDDFT dynamics over 5 ps and using a larger ensemble of 50 trajectories. Since the two lowest excited states cross and exchange their electronic diabatic character close to the initial ground state geometry, each trajectory has been initiated in the state that is bright at the given initial geometry. The time-dependent excited state populations obtained from the nonadiabatic dynamics (cf.

Fig. 7) do not exhibit simple ultrafast decay but undergo strong oscillations due to the large coupling between the S_1 and S_2 state and their almost degeneracy. No relaxation to the

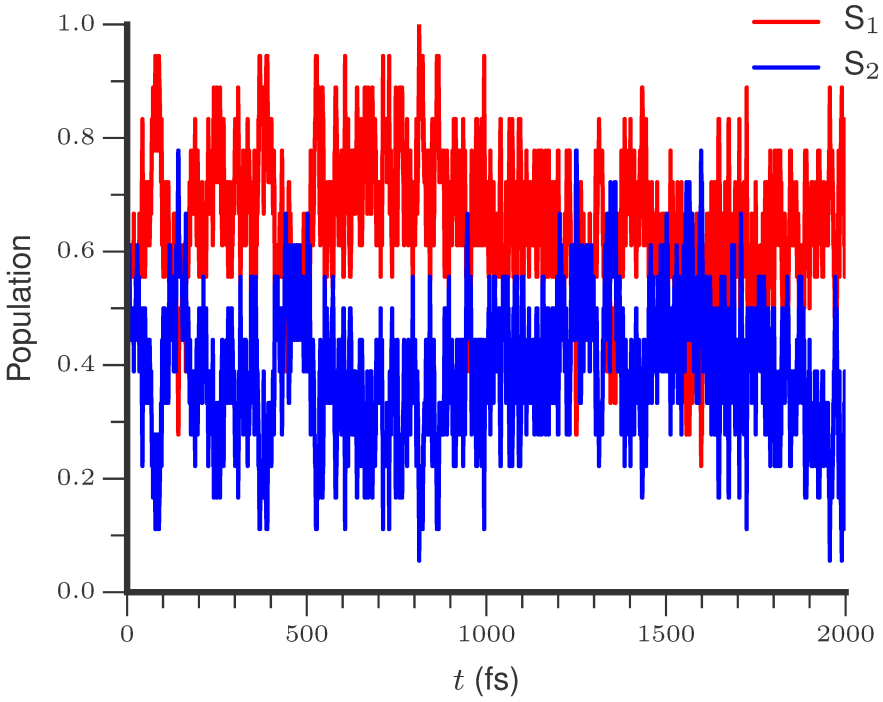

Figure 7: Time-dependent populations of the S_2 and S_1 states obtained from the surface hopping nonadiabatic dynamics simulations.

electronic ground state has been observed during the simulation time, which is consistent with the observed fluorescence of pyrene dimer. Based on the results of the nonadiabatic dynamics simulations, two distinct excimer formation channels have been identified in the gas phase: Depending on the initial energy and the geometry distortion, the trajectories either remain trapped close to the FC region and undergo vibrational dynamics mainly along the intermolecular stacking coordinate as the excimer state is formed, or they undergo large amplitude motion towards the perfectly stacked global minimum in the first excited state along the parallel shift coordinate which is accompanied by a simultaneous decrease of the perpendicular distance. Both relaxation channels can be qualitatively understood based on the shape of the potential energy surfaces shown in Fig. 5 that exhibit a local minimum close to the FC geometry and a global minimum at the perfectly stacked geometry. As an

illustration, the excited state energies along a single trajectory that undergoes the parallel shift are presented in Fig. 8a. After initial excitation, the trajectory shown in Fig. 8a

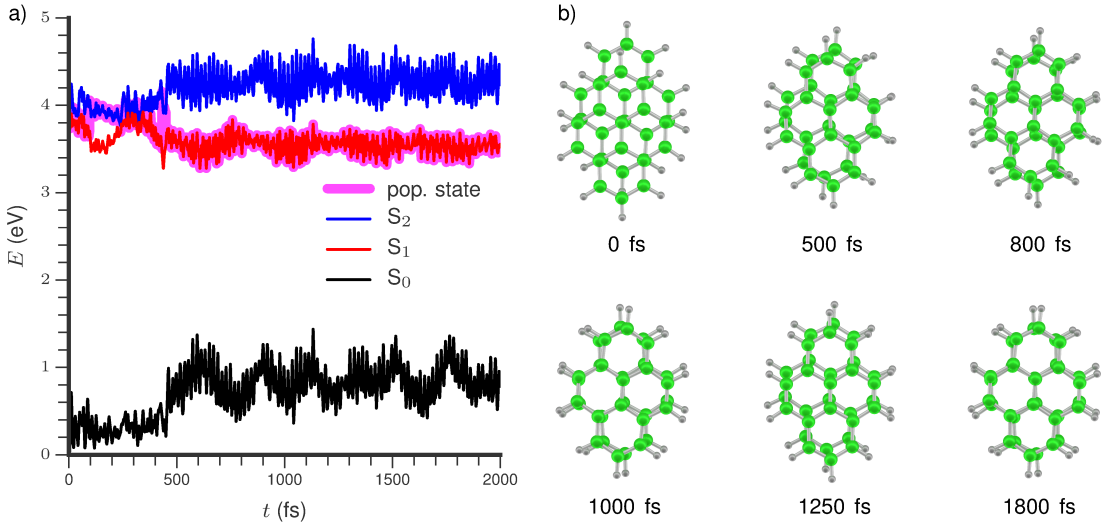

Figure 8: (a) Energies of the ground and two lowest excited states along a typical nonadiabatic trajectory exhibiting parallel shift towards the perfectly stacked structure. The thick magenta colored curve marks the state in which the trajectory resides. (b) Snapshots of the geometries along the same trajectory for selected times.

switches between the S_2 and S_1 state within the first 500 fs while the two pyrene monomers slide along the parallel shift coordinate as can be seen from the dynamics snapshots shown in Fig 8b. After approximately 1 ps the perfectly stacked structure is reached for the first time and the energy gap between the S_1 and S_2 opens. Since the energy is only slowly dissipated away from the parallel shift coordinate the trajectory overshoots the stacked structure and exhibits damped oscillations about the global minimum geometry which persist for at least 2 ps. As already mentioned, the opening of the energy gap can be largely attributed to the increase in the short-range coupling at the stacked geometry due to the favorable orbital overlap. The other part of the trajectory ensemble (not shown), remains trapped close to the FC geometry and switches back and forth between both excited states as it passes the crossing region. In all trajectories, the perpendicular distance between the monomer units decreases with time as can be seen from Fig. 9 reflecting the stronger binding in the excited state which is a characteristic of the excimer formation.

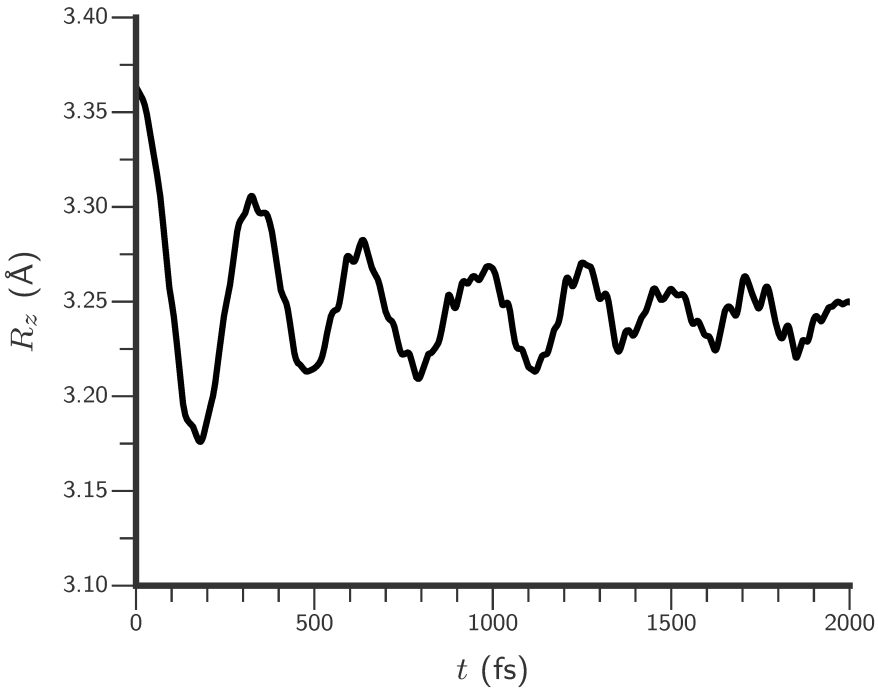

Figure 9: Stacking distance between the pyrene monomers as a function of time averaged over an ensemble of surface hopping trajectories.

The stabilization of the excimer requires the removal of energy from the stacking coordinate and its internal redistribution over all available vibrational modes. Thus, the excimer formation time is intimately connected with the rate of energy dissipation from the initially excited stacking and parallel shift coordinate into other (bath) modes. The time-scale for the internal energy redistribution can be inferred from Fig. 9 where we plot the average stacking distance for the whole trajectory ensemble as a function of time. Initially, the stacking distance drops from 3.36 Å to 3.18 Å within the first 100 fs and exhibits subsequently damped oscillations with a period of $\approx$ 350 fs that persist for the whole simulation time of 2 ps. Since the full TDDFT nonadiabatic dynamics cannot be extended beyond 2 ps due to the high computational demand, we have performed more approximate TDDFTB simulations over a longer time span. The TDDFTB simulations (see Fig. S6) show that the oscillations fully decay on a time-scale of $\approx$ 5 ps. Thus, we can conclude that the excimer stabilization in the gas-phase pyrene dimer occurs on a time-scale of $\approx$ 5 ps and is largely

governed by the efficiency of the intramolecular energy redistribution. In the following we

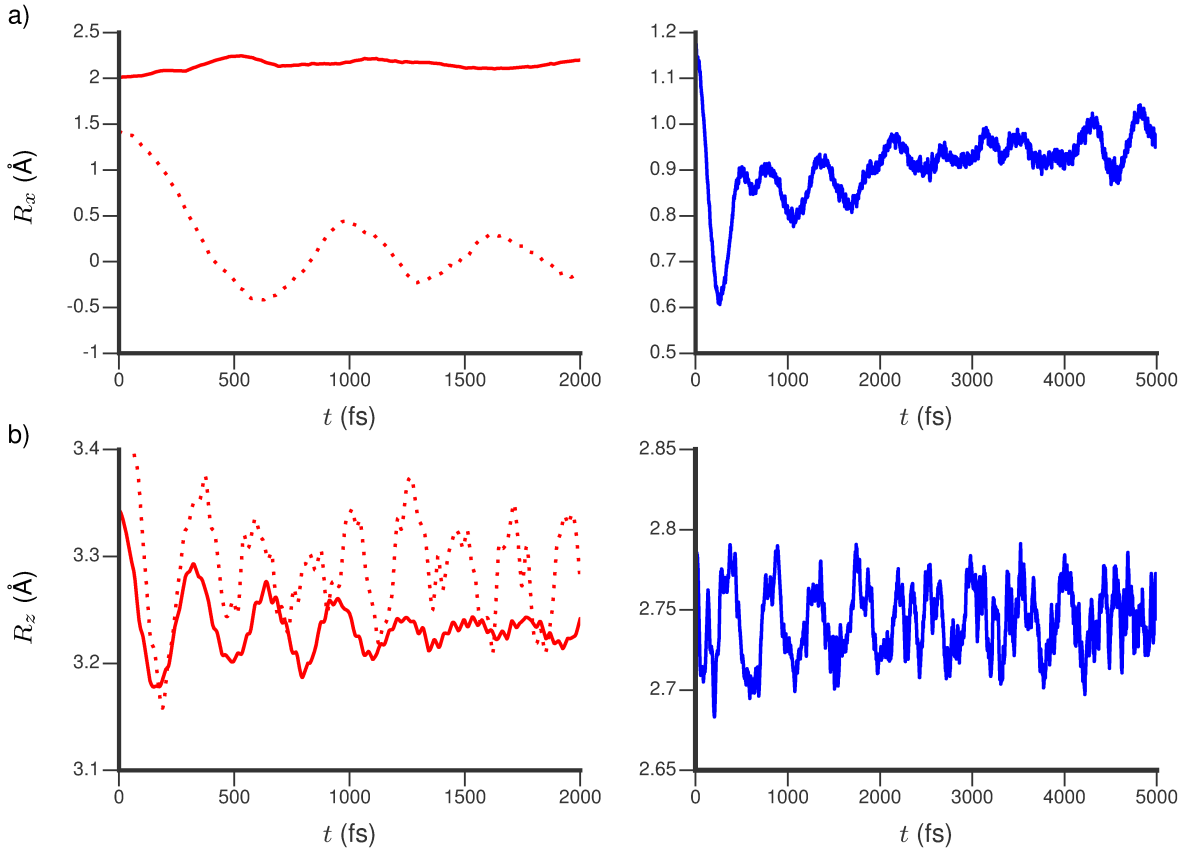

Figure 10: (a) Average value of the parallel shift coordinate R_x as a function of time for the gas phase pyrene dimer (red) and for pyrene dimer embedded in a crystal environment (blue). The gas phase values have been divided into two excimer forming channels as described in text (full and dashed red lines). (b) Average stacking distance as a function of time. Labelling is the same as in part a).

explore the influence of the crystal environment on the excimer formation in the frame of QM/MM nonadiabatic dynamics simulations on a pyrene crystal model in the frame of the long-range corrected TDDFTB.

The excited state dynamics in the crystal environment exhibits several differences with respect to the gas phase dynamics. We present in Fig. 10 average values of the parallel shift and perpendicular distance coordinates obtained from the gas phase and crystal nonadiabatic dynamics. The gas phase results have been separated into two excimer formation channels described above (cf. full and dashed red curves in Figs. 10a and c). In contrast

to the dynamics in the gas phase, the oscillation in the parallel shift coordinate is faster and more strongly damped in the crystal environment. Within the first 300 fs the parallel shift coordinate decreases rapidly from 1.2 Å to about 0.6 Å. This leads to a collision with the neighboring molecules in the crystal and almost impulsive energy transfer to the surroundings which is followed by a slower relaxation with the shift reaching the value of 1.0 Å after 5 ps. The differences are also visible in the time-dependence of the stacking coordinate which is shown in Fig. 10b. Notice, that the stacking coordinate have generally lower value in the TDDFTB simulations due to the overestimation of the dispersion energy. The stacking coordinate exhibits oscillations that persist over the whole period of 5 ps and are less damped than in the gas phase case. This is due to the absence of the second excimer formation channel that involves significant parallel shift and leads to stronger damping in the gas phase simulation. In fact, when compared to the gas phase relaxation channel that does not involve parallel shift (dashed red line in Fig. 10) the period of the oscillation and damping are similar both in the gas phase and in the crystal. As an illustration of the crystal dynamics we present in Fig. 11a structures sampled from a single nonadiabatic trajectory over the time interval of 5 ps as well as the electronic state energies as a function of time in Fig. 11b. After initial excitation of the S_1 exciton state, a fast opening of the energy gap between the excited states is observed within the first 300 fs that accompanies the motion along the parallel shift coordinate. After the collision with the surrounding environment, the gap becomes again smaller and continues to fluctuate over the whole simulation period.

Conclusion

We carried out a joint experimental and theoretical study of the ultrafast excimer formation dynamics in pyrene dimer, arguably the most important model for excimer photophysics in general. The nonadiabatic dynamics was simulated in the frame of TDDFT and combined with time-resolved picosecond ionization experiments. The simulations in the gas phase

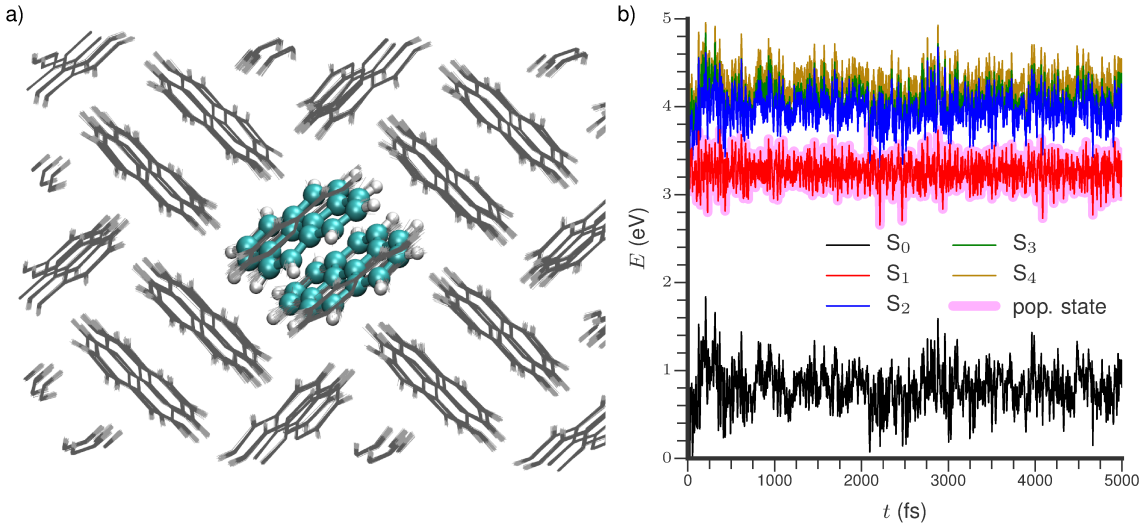

Figure 11: (a) Section from the QM/MM model for for nonadiabatic dynamics of pyrene dimer in a crystal. In the figure structures from a single nonadiabatic trajectory have been superposed. (b) Ground and excited state energies of pyrene dimer (QM part of the model) as a function of time. The thick magenta line labels the occupied state during the surface hopping simulation.

led to the identification of two excimer formation channels involving: (i) local relaxation along the stacking coordinated close to the FC window and (ii) large amplitude oscillations along the parallel shift coordinate accompanied by damped oscillations along the stacking direction. Both processes lead to the stabilization of the excimer on a time scale of ≈ 5 ps. The excited state dynamics is characterized by a strong coupling between the two lowest exciton states due to the presence of conical intersections between the delocalized excitonic states. Such conical intersections arise due to the interplay between the long-range and short-range electronic coupling and may play an important role in the excited state dynamics in materials containing stacked π-conjugated systems. The simulations were supported by the picosecond photoionization experiments in a supersonic jet that reveal excited state dynamics with a time constant of 6-8 ps that is assigned to excimer formation. Experimental and computed time constant are thus in a very good agreement. The redistribution of vibrational energy in the excited state upon excimer formation leads to a change in the ionization probability that manifests itself in a transient contribution to the ion signal. Experiments

were conducted at several excitation wavelength and dissociative photoionization of larger clusters was successfully suppressed in most experiments.

In addition to the experimental and theoretical study of the gas phase dynamics we also explored the influence of the crystal environment on the excimer formation with the help of QM/MM tight-binding TDDFT nonadiabatic dynamics simulations on a crystal model. The excimer formation in the crystal environment proceeds along a single pathway that involves strongly damped motion along the parallel shift coordinate accompanied by oscillations along the stacking direction decaying on a time scale larger than 5 ps. Our findings provide a first detailed picture of the excimer formation dynamics and show that dynamical effects should play an important role in the design of novel organic functional materials. The function of even perfectly structurally designed molecular material may rapidly deteriorate due to the ultrafast excimer formation mediated by the efficient nonradiative processes at conical intersections.

Acknowledgement

JH, AH, RM and MISR gratefully acknowledge the financial support by the European Research Council (ERC) Consolidator grant DYNAMO (Grant Nr. 646737). IF would like to thank the German Science Foundation, DFG for funding via project FI575/9-x. HCS acknowledges a fellowship by the Fonds der Chemischen Industrie.

Supporting Information Available

This will usually read something like: "Experimental procedures and characterization data for all new compounds. The class will automatically add a sentence pointing to the information on-line:

This material is available free of charge via the Internet at `http://pubs.acs.org/`.

References

(1) Förster, T. *Angew. Chem. Int. Ed.* **1969**, *8*, 333–343.

(2) Klopffer, W.; Birks, J. *Organic Molecular Photophysics*; 1973; pp 357–402.

(3) Lim, J. M.; Kim, P.; Yoon, M.-C.; Sung, J.; Dehm, V.; Chen, Z.; Wurthner, F.; Kim, D. *Chem. Sci.* **2013**, *4*, 388–397.

(4) Marciniak, H.; Li, X.-Q.; Würthner, F.; Lochbrunner, S. *Phys. Chem. A* **1010**, *115*, 648.

(5) Ye, T.; Singh, R.; Butt, H.-J.; Floudas, G.; Keivanidis, P. E. *ACS Appl. Mater. Interfaces* **2013**, *5*, 11844.

(6) Chen, Z.; Stepanenko, V.; Dehm, V.; Prins, P.; Siebbeles, L. D. A.; Seibt, J.; Marquetand, P.; Engel, V.; Würthner, F. *Chem. Eur. J.* **2007**, *13*, 436.

(7) Howard, I. A.; Laquai, F. D. R.; Keivanidis, P. E.; Friend, R. H.; Greenham, N. C. *J. Phys. Chem. C* **2009**, *113*, 21225.

(8) Smith, M. B.; Michl, J. *Annu. Rev. Phys. Chem.* **2013**, *64*, 361–386.

(9) Mauck, C. M.; Hartnett, P. E.; Margulies, E. A.; Ma, L.; Miller, C. E.; Schatz, G. C.; Marks, T. J.; Wasielewski, M. R. *J. Am. Chem. Soc.* **2016**, *138*, 11749–11761.

(10) Beljonne, D.; Yamagata, H.; Brédas, J. L.; Spano, F. C.; Olivier, Y. *Phys. Rev. Lett.* **2013**, *110*, 226402.

(11) Walker, B. J.; Musser, A. J.; Beljonne, D.; Friend, R. H. *Nat. Chem.* **2013**, *5*, 1019.

(12) Eaton, S. W.; Shoer, L. E.; Karlen, S. D.; Dyar, S. M.; Margulies, E. A.; Veldkamp, B. S.; Ramanan, C.; Hartzler, D. A.; Savikhin, S.; Marks, T. J. *J. Am. Chem. Soc.* **2013**, *135*, 14701.

(13) Chen, S.; Wang, L.; Fahmi, N. E.; Benkovic, S. J.; Hecht, S. M. *J. Am. Chem. Soc.* **2012**, *134*, 18883–18885.

(14) Santiago-Gonzalez, B.; Monguzzi, A.; Azpiroz, J. M.; Prato, M.; Erratico, S.; Campione, M.; Lorenzi, R.; Pedrini, J.; Santambrogio, C.; Torrente, Y. *Science* **2016**, *353*, 571–575.

(15) Jumper, C. C.; Anna, J. M.; Stradomska, A.; Schins, J.; Myahkostupov, M.; Prusakova, V.; Oblinsky, D. G.; Castellano, F. N.; Knoester, J.; Scholes, G. D. *Chem. Phys. Lett.* **2014**, *599*, 23–33.

(16) Musser, A. J.; Liebel, M.; Schnedermann, C.; Wende, T.; Kehoe, T. B.; Rao, A.; Kukura, P. *Nat. Phys.* **2015**, *11*, 352–357.

(17) Förster, T.; Kasper, K. *Berichte der Bunsengesellschaft für physikalische Chemie* **1955**, *59*, 976–980.

(18) Saigusa, H.; Lim, E. C. *Acc. Chem. Res.* **1996**, *29*, 171–178.

(19) Miyasaka, H.; Masuhara, H.; Mataga, N. *J. Phys. Chem.* **1985**, *89*, 1631–1636.

(20) Saigusa, H.; Lim, E. C. *Chem. Phys. Lett.* **2001**, *336*, 65–70.

(21) Willberg, D.; Gutmann, M.; Breen, J.; Zewail, A. *J. Chem. Phys.* **1992**, *96*, 198–212.

(22) Hertel, I.; Radloff, W. *Rep. Prog. Phys.* **2006**, *69*, 1897.

(23) Knochenmuss, R.; Fischer, I.; Lührs, D.; Lin, Q. *Isr. J. Chem.* **1999**, *39*, 221–230.

(24) Lührs, D. C.; Knochenmuss, R.; Fischer, I. *Phys. Chem. Chem. Phys.* **2000**, *2*, 4335–4340.

(25) Piuzzi, F.; Dimicoli, I.; Mons, M.; Millié, P.; Brenner, V.; Zhao, Q.; Soep, B.; Tramer, A. *Chem. Phys.* **2002**, *275*, 123–147.

(26) Miyazaki, M.; Fujii, M. *Phys. Chem. Chem. Phys.* **2015**, *17*, 25989–25997.

(27) Birks, J. *Rep. Prog. Phys.* **1975**, *38*, 903.

(28) Andriessen, R.; Ameloot, M.; Boens, N.; De Schryver, F. C. *J. Phys. Chem.* **1992**, *96*, 314–326.

(29) Becke, A. *Phys. Rev. A* **1988**, *38*.

(30) Lee, C.; Yang, W.; Parr, G. R. *Phys. Rev. B.* **1988**, *37*, 785.

(31) Becke, A. D. *J. Chem. Phys.* **1993**, *98*, 1372.

(32) Schäfer, A.; Huber, C.; Ahlrichs, R. *J. Chem. Phys.* **1994**, *100*, 2975.

(33) Grimme, S.; Antony, J.; Ehrlich, S.; Krieg, H. *J. Chem. Phys.* **2010**, *132*, 154104.

(34) Huenerbein, R.; Grimme, S. *Chemical Physics* **2008**, *343*, 362.

(35) Weigend, F.; Häser, M.; Patzelt, H.; Ahlrichs, R. *Chem. Phys. Letters* **1988**, *294*, 143.

(36) TURBOMOLE V6.3 2010, a development of University of Karlsruhe and Forschungszentrum Karlsruhe GmbH, 1989-2007, TURBOMOLE GmbH, since 2007; available from
`http://www.turbomole.com`.

(37) Werner, U.; Mitrić, R.; Bonačić-Koutecký, V. *Chem. Phys.* **2008**, *349*, 319.

(38) Mitrić, R.; Werner, U.; Bonačić-Koutecký, V. *J. Chem. Phys.* **2009**, *129*, 164118.

(39) Mitrić, R.; Werner, U.; Wohlgemuth, M.; Seifert, G.; Bonačić-Koutecký, V. *J. Phys. Chem. A* **2009**, *113*, 12700.

(40) Lisinetskaya, P. G.; Mitric, R. *Phys. Rev. A* **2011**, *83*, 033408.

(41) Mayo, S.; Olafson, B.; Goddard III, W. *J. Phys. Chem.* **1990**, *94*, 8897.

(42) Schon, C.; Roth, W.; Fischer, I.; Pfister, J.; Kaiser, C.; Fink, R. F.; Engels, B. *Phys. Chem. Chem. Phys.* **2010**, *12*, 9339.

(43) Auerswald, J.; Engels, B.; Fischer, I.; Gerbich, T.; Herterich, J.; Krueger, A.; Lang, M.; Schmitt, H.-C.; Schon, C.; Walter, C. *Phys. Chem. Chem. Phys.* **2013**, *15*, 8151.

(44) Mangle, E. A.; Topp, M. R. *J. Phys. Chem.* **1986**, *90*, 802–807.

(45) Numata, Y.; Nirasawa, T.; Suzuka, I. *J. Photochem. Photobiol., A* **2010**, *209*, 27–31.

(46) Ohta, N.; Baba, H.; Marconi, G. *Chem. Phys. Lett.* **1987**, *133*, 222–229.

(47) Zhang, J.; Han, F.; Kong, W. *J. Phys. Chem. A* **2010**, *114*, 11117–11124.

(48) Joblin, C. personal communication.

(49) Cheng, K. A. W. Y.; Schepp, N. P.; Cozens, F. L. *J. Phys. Chem. A* **2004**, *108*, 7132–7134.

(50) Costa, T.; Seixas de Melo, J. S.; Castro, C. S.; Gago, S.; Pillinger, M.; Goncalves, I. S. *J. Phys. Chem. B* **2010**, *114*, 12439.

(51) Hsu, C. P.; You, Z. Q.; Chen, H. C. *J. Phys. Chem. C* **2008**, *112*, 1204.

(52) Arago, J.; Troisi, A. *Phys. Rev. Lett.* **2015**, *114*, 026402.

(53) Koutecký, J.; Paldus, J. *Theoret. Chim. Acta* **1963**, *1*, 268–281.

(54) Madjet, M. A. E.; Abdurahman, A.; Renger, T. *J. Phys. Chem. B* **2006**, *110*, 17268.

(55) Scholes, G. D.; Gould, I.; Cogdell, R.; Fleming, G. R. *J. Phys. Chem. B* **1999**, *110*, 17268.

(56) Madjet, M. E. A.; Müh, F.; Renger, T. *J. Phys. Chem. B* **2009**, *113*, 12603.

Graphical TOC Entry